RESEARCH ARTICLE

National Science Review
10: nwad245, 2023
https://doi.org/10.1093/nsr/nwad245
Advance access publication 13 September 2023

MATERIALS SCIENCE

Photoexcitation-induced passivation of SnO_2 thin film for efficient perovskite solar cells

Nianyao Chai[1,†], Xiangyu Chen[1,†], Zhongle Zeng[1], Ruohan Yu[1], Yunfan Yue[1], Bo Mai[1], Jinsong Wu[1], Liqiang Mai[1,2,*], Yi-Bing Cheng[1,2] and Xuewen Wang[1,2,*]

ABSTRACT

A high-quality tin oxide electron transport layer (ETL) is a key common factor to achieve high-performance perovskite solar cells (PSCs). However, the conventional annealing technique to prepare high-quality ETLs by continuous heating under near-equilibrium conditions requires high temperatures and a long fabrication time. Alternatively, we present a non-equilibrium, photoexcitation-induced passivation technique that uses multiple ultrashort laser pulses. The ultrafast photoexcitation and following electron–electron and electron–phonon scattering processes induce ultrafast annealing to efficiently passivate surface and bulk defects, and improve the crystallinity of SnO_2, resulting in suppressing the carrier recombination and facilitating the charge transport between the ETL and perovskite interface. By rapidly scanning the laser beam, the annealing time is reduced to several minutes, which is much more efficient compared with conventional thermal annealing. To demonstrate the university and scalability of this technique, typical antisolvent and antisolvent-free processed hybrid organic–inorganic metal halide PSCs have been fabricated and achieved the power conversion efficiency (PCE) of 24.14% and 22.75% respectively, and a 12-square-centimeter module antisolvent-free processed perovskite solar module achieves a PCE of 20.26%, with significantly enhanced performance both in PCE and stability. This study establishes a new approach towards the commercialization of efficient low-temperature manufacturing of PSCs.

Keywords: photoexcitation-induced passivation, ultrafast laser, carrier management, electron transport layer, perovskite solar cells

[1]State Key Laboratory of Advanced Technology for Materials Synthesis and Processing, International School of Materials Science and Engineering, Wuhan University of Technology, Wuhan 430070, China and [2]National Energy Key Laboratory for New Hydrogen-Ammonia Energy Technologies, Foshan Xianhu Laboratory, Foshan 528000, China

***Corresponding authors.** E-mails: xwwang@whut.edu.cn; mlq518@whut.edu.cn

[†]Equally contributed to this work.

Received 11 July 2023; **Revised** 29 August 2023; **Accepted** 10 September 2023

INTRODUCTION

Inorganic metal oxide semiconductors are widely used as electron transport layers (ETLs) for perovskite solar cells (PSCs), which efficiently extract and transport electrons from the perovskite layer into the electrode [1–5]. Tin (IV) oxide (SnO_2)-based ETLs offer desirable band alignment and electron mobility, while being processable at much lower temperatures [6,7]. Among various deposition methods [8–10], SnO_2 nanoparticle-based PSCs prepared by using chemical bath deposition (CBD), which provides conformal coverage between the perovskite layer and the electrode, have demonstrated the best performance so far [11–13]. However, the intrinsic defects (e.g. oxygen vacancies, tin interstitials) and surface defects (e.g. hydroxyl groups and Sn dangling bonds) that are unavoidably formed in SnO_2 generate massive shallow trap states near the conduction band and result in carrier recombination at the SnO_2/perovskite interface [14,15]. To reduce the carrier loss, the ETL film prepared by using CBD generally requires an annealing condition with a temperature of ≥170°C for ≥1 hour [11–13,16]. This is in part because the ETLs normally show poor heat transfer and large thermal inertia for passivation under near thermal equilibrium, which makes it challenging to reduce the annealing temperature and time, bringing additional energy costs. Currently, except for thermal annealing at high temperatures for at least 1 h, there is no better way to reduce the annealing temperature of tin oxide films prepared by using the CBD method [17,18]. At the same time, thermal

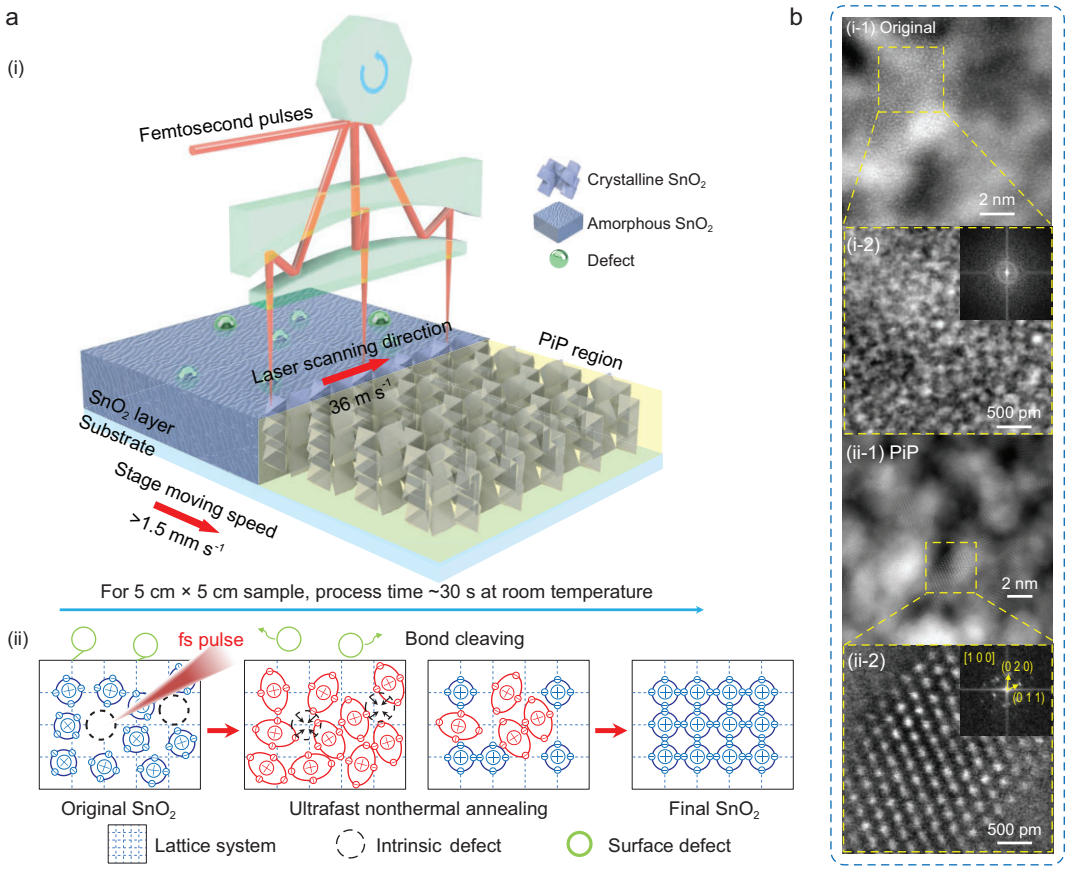

Figure 1. Diagram of the photoexcitation-induced ultrafast passivation (PiP) process and phase transition of SnO_2 thin films. (a) Schematic of the PiP procedure during the annealing of SnO_2 thin films and the specific mechanisms of the annealing process including photoexcitation, electron–electron and electron–phonon scattering, rearrangement of atoms and defects passivation. (b) High-resolution TEM images of (i) original-SnO_2 and (ii) PiP-SnO_2 (the insets show fast Fourier transform patterns of the TEM images).

annealing is generally followed by buried interface passivation to further reduce surface defects, which requires additional thermal annealing and complicates the preparation process [19,20].

Herein, we report a novel non-equilibrium, photoexcitation-induced passivation (PiP) technique that uses ultrashort laser pulses. The ultrafast photoexcitation and following electron–electron and electron–phonon scattering processes induce an ultrafast electron and phonon heating process, thus ensuring efficient low-temperature annealing of SnO_2 nanoparticle-based ETLs prepared by using CBD. By rapidly scanning a laser beam, the annealing process of a 5 cm × 5 cm sample can be finished within 30 s at room temperature, which facilitates the scale-up and energy saving of fabricating PSCs. The two representative perovskite-based PSCs fabricated via this method achieve a great enhancement in comparison with the control devices, and a power conversion efficiency (PCE) of 20.26% for a 12-square-centimeter perovskite solar module (PSM) is achieved as well.

RESULT AND DISCUSSION

PiP of SnO_2 thin film

The schematic of a home-built PiP set-up and the mechanism of PiP are shown in Fig. 1a. A femtosecond laser beam is reflected by a high-speed rotating polygon mirror and then focused on the sample. The set-up has a laser scanning speed of >36 m s^{-1} in a working range of 300 mm, with a stage movement speed of >1.5 mm s^{-1}, which ensures annealing a 5 cm × 5 cm sample in 30 s and a 10 cm × 10 cm sample in 60 s, as shown in Fig. 1a (i). The detailed home-built PiP experimental set-up can be found in the Methods and Supplementary material. The demonstration and actual processing video can be found in the Supplementary movie.

The PiP process is achieved by using ultrafast intensive excitation after laser pulse energy deposition in tens of femtoseconds, followed by the electron–electron and electron–phonon scattering processes (in hundreds of femtoseconds), as shown in Fig. 1a (ii). The interaction between the ultrafast laser and

the SnO_2 film starts from direct photon absorption by excitation of intrinsic free carriers and shallow trap states. The absorption coefficient is 1650 cm^{-1} at 1030 nm as measured. The carrier population will rapidly rise up to the anti-bonding states (conduction band) by impact ionization via the electron–electron scattering process in tens of femtoseconds. The population of anti-bonding states raises the free energy of the excited system, generating a stretching force on each bond, which efficiently cleaves weak or metastable bonds, thus passivating the surface defects and oxygen vacancies of the SnO_2 film [21–23].

The following electron–phonon scattering process to reach an equilibrium temperature of the electron and phonon system induces an ultrafast phonon heating process (for 28 mJ cm^{-2} laser fluence, the maximum temperature rise is 22.6 K) with a heating rate of $>10^{13}$ K s^{-1} in hundreds of femtoseconds (see the Supplementary material for theoretical analysis of temperature rise by PiP) and an ultrafast thermal gradient with the Gaussian distribution is generated in the focus zone (Supplementary Fig. S1a) [24]. On the way to cooling the excited system, atoms obtain excessive kinetic energy to align into an ordered arrangement, thus passivating the bulk defects of the SnO_2 and improving the crystallinity of the SnO_2 [21,25]. This temperature gradient decays rapidly via thermal diffusion in 25 ns with a quenching rate of $\sim 10^9$ K s^{-1}. The accumulation temperature after 50 consecutive laser pulses is only 6.5 K (Supplementary Fig. S1b), showing that the temperature rise after each single pulse drops to near room temperature before the next pulse arrives, demonstrating that the accumulation effect is negligible in the PiP process of the SnO_2 film. This shows that the whole passivation process is completed very fast with much more energy and time efficiency compared with the conventional annealing technique.

The microscopic characterization of the SnO_2 thin film cross sections using high-resolution transmission electron microscope (HRTEM) and the corresponding energy-disperse X-ray spectroscopy of Sn, O, F and Pt (Supplementary Fig. S2) present a complete coverage over the fluorine-doped tin oxide (FTO) surface. By comparing the HRTEM images before and after the PiP, it is found that a large number of amorphous particles existed in the original SnO_2 (Fig. 1b, part i-1). This is more clearly identified from the random distribution of Sn atoms in the atomic-resolution image and the corresponding fast Fourier transform (FFT) pattern (Fig. 1b, part i-2). More representative HRTEM images of the original SnO_2 are shown in Supplementary Fig. S3. As shown in Fig. 1b, part ii-1, the PiP process leads to the SnO_2 undergoing a transformation from the amorphous phase to the crystalline phase, thus improving the crystallinity of the SnO_2, which is confirmed by the massive appearance of lattice fringes and regularly arranged Sn atoms. The FFT pattern of the SnO_2 atomic-resolution image (Fig. 1b, part ii-2) after PiP corresponds to the [100] zone axes. More representative HRTEM images of the SnO_2 after the PiP are shown in Supplementary Fig. S4.

Morphology, optoelectronic properties and surface defect characterization of SnO_2 films

To investigate the reasons why the PiP-SnO_2 thin film efficiently improves the cell performance, the surface morphology of SnO_2 thin films was studied by using scanning electron microscopy (SEM) images, as shown in Fig. 2a. Compared with the smooth, bare FTO surface, the SnO_2 thin film deposited on the FTO is composed of compact nanoparticles. All SnO_2 thin films are uniform and full-coverage except for the much higher laser fluence. This is because at high laser fluence, SnO_2 nanoparticles tend to coalesce into large crystallites, resulting in pinholes in the SnO_2 thin films. These large crystallites and pinholes act as carrier trap sites in the SnO_2/perovskite interface where the energy is lost through non-radiative recombination pathways, resulting in a reduction in carrier lifetimes. The contact angle first increases with increasing laser fluence (Fig. 2b), which indicates a reduction in surface hydrophilic groups. However, when the laser fluence is further increased, the non-uniformity of the surface increases the hydrophilicity. The transmittance spectra of the original-SnO_2, 170°C thermal-annealed SnO_2 for 1 hour (170°C-SnO_2) and PiP-SnO_2 thin films on FTO substrates are shown in Fig. 2c and Supplementary Fig. S5a. There is a slight increase in the transmittance of the substrate with the PiP-SnO_2 thin films, which could contribute to the high J_{SC} of the PSCs. Since the SnO_2 thin film is very thin relative to the FTO layer, there is no clear difference in transmittance. The conductivity of the SnO_2 thin films on the FTO shows an increase of >20% by the PiP (Fig. 2d and Supplementary Fig. S5b). Moreover, the electron mobility of various ETLs measured by using a space charge-limited current method is shown in Supplementary Fig. S6 [26]. It can be found that the electron mobility of the SnO_2 is higher than that of the original-SnO_2 and 170°C-SnO_2, which is beneficial to SnO_2 thin films to transport electrons generated from the perovskite layer, thereby improving the cell performance.

Since the film deposition takes place in a water-based solution, OH groups (surface defects) inevitably appear in the SnO_2 thin film, which is

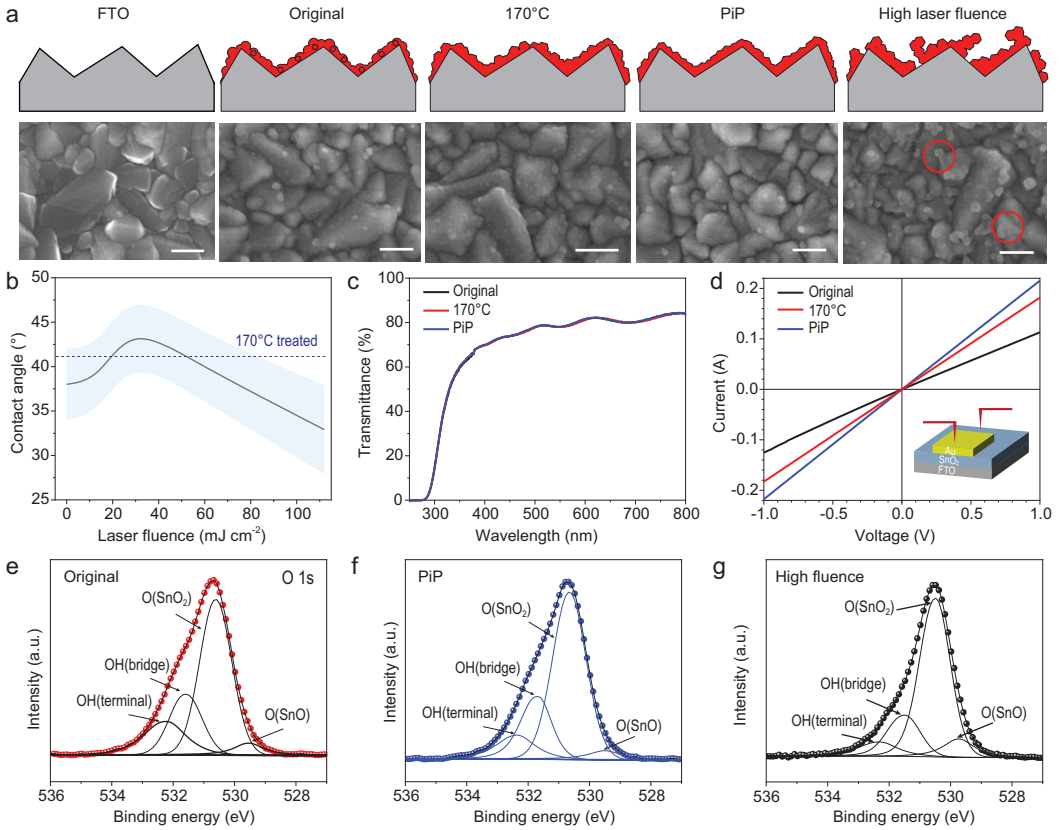

Figure 2. Characterization of SnO_2 films. (a) Schematic illustration of morphologic change of original-SnO_2, 170°C-SnO_2 and PiP-SnO_2 thin films on FTO substrate and corresponding top-view SEM. Scale bars are 200 nm. Comparison of (b) contact angle, (c) transmittance spectra and (d) conductivity of the original-SnO_2, 170°C-SnO_2 and PiP-SnO_2 thin films on the FTO substrate. (e–g) The XPS spectrum of O1s of original-SnO_2, PiP-SnO_2 and high-laser-fluence-treated SnO_2 thin films.

proved by the X-ray photoelectron spectrum (XPS) in Fig. 2e–g and Supplementary Fig. S7a. After the calibration of the spectra by using the C1s peak, the deconvolution of the O1s peak was executed in detail to detect the four oxygen species for each sample. Generally, there are two kinds of OH groups commonly existing on the SnO_2 thin film surface [27]. One is $OH_{(bridge)}$ integrated with two metal sites at 531.5 (±0.1) eV and the other is $OH_{(terminal)}$, which binds to one metal site at 532.2 (±0.1) eV [27–29]. The relative proportions of $OH_{(bridge)}$ and $OH_{(terminal)}$ species for each sample are listed in Supplementary Table S1. The relative proportions of $OH_{(bridge)}$ and $OH_{(terminal)}$ decrease both for 170°C-SnO_2 and PiP-SnO_2 thin films, which indicates that the PiP achieves a similar effect to conventional high-temperature thermal annealing. Compared with the 170°C annealing for 1 hour, the PiP is much more time-efficient. From the XPS results, we can confirm that the PiP process can not only drive the SnO_2 undergoing a phase transition from the amorphous state to the crystalline state, but also reduce the metastable surface functional groups on SnO_2 thin films, as shown in Supplementary Fig. S7b. The metastable $OH_{(bridge)}$ and $OH_{(terminal)}$ could be cleaving after photoexcitation, which is also indicated by the enhanced Raman peak at 632 cm^{-1} (corresponding to the fundamental active Raman vibration modes A_{1g}) in Supplementary Fig. S8 [30,31].

Carrier transport behaviors between SnO_2 films and perovskite films

An ideal band alignment is critical to efficiently extracting electrons from perovskite to ETL and preventing hole quenching at the ETL/perovskite interface [15,32,33]. As shown in Fig. 3a, the first principle density functional theory (DTF) calculations reveal that the removal of metastable surface OH groups reduces the conduction band minimum, facilitating charge extraction. At the same time, it increases the valence band maximum, so as to efficiently transfer electrons and block holes (Supplementary Fig. S9) [7]. Ultraviolet photoelectron spectroscopy (UPS) supports that the deeper valence band is achieved (Fig. 3b) [34]. Steady-state photoluminescence (PL) and

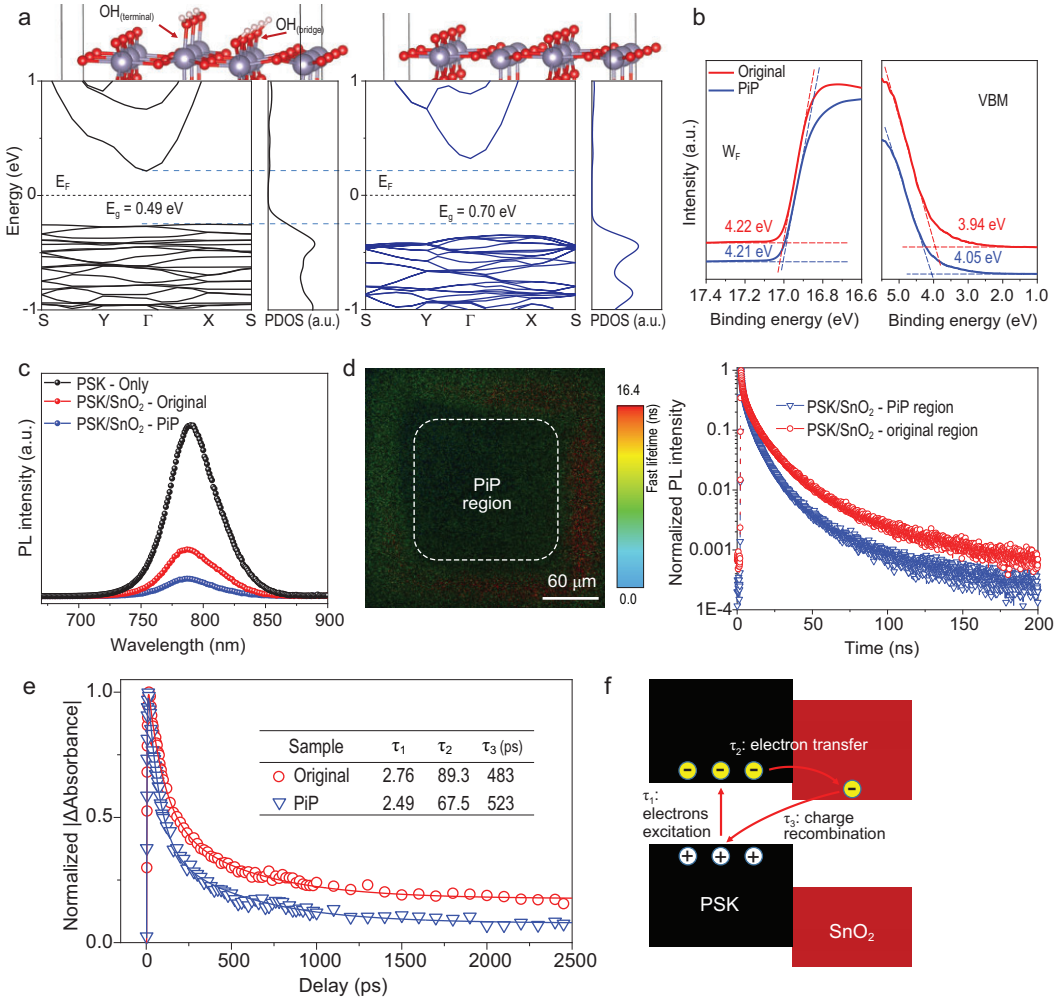

Figure 3. Influence of PiP of SnO_2 on its band alignment with perovskite and the carrier transfer processes at the interface of the SnO_2 and the perovskite. (a) Band structure and partial density of states of original-SnO_2 and PiP-SnO_2. (b) The energy onset and cut-off of UPS spectra of original-SnO_2 and PiP-SnO_2 thin films, respectively, where their work function and valence band maximum can be derived. (c) Steady-state photoluminescence (PL) spectral photon flux for the perovskite film with different ETLs. (d) Time-resolved confocal PL lifetime map and corresponding time-resolved PL traces for selective PiP SnO_2-based perovskite film. (e) Transient absorption decay kinetic traces of SnO_2/perovskite at 750 nm. The kinetic analyses with three-exponential fit are also shown by solid lines. (f) Schematic diagram of the overall photocarrier dynamics between the SnO_2 and the perovskite.

time-resolved photoluminescence (TRPL) measurements were also carried out to probe the photocarrier dynamics between the SnO_2 layers and the perovskite layer (Fig. 3c and Supplementary Fig. S10). The crystallinity of the deposited perovskite film on different SnO_2 films is consistent, which is confirmed by the results of X-ray diffraction (XRD) analysis (Supplementary Fig. S11). The PiP-SnO_2/perovskite film has a lower PL intensity and shorter carrier lifetime than the other films. Time-resolved confocal PL lifetime mapping of selectively annealed SnO_2 by PiP-based perovskite film and the TRPL spectra of the corresponding region demonstrate the more efficient electron extraction after the PiP (Fig. 3d). The dotted box in the middle is the selectively PiP-SnO_2/perovskite region, which exhibits a shorter PL lifetime than the original part. These results further support the reduction in charge recombination in the PiP-SnO_2/perovskite interface. To further investigate the photocarrier dynamics at the ETL/perovskite interface, femtosecond transient absorption spectroscopy was employed, as shown in Supplementary Fig. S12, to show the time-resolved difference absorption spectra in the 10 ps–1 ns timescale of different SnO_2/perovskite films. The amplitude of the ground-state bleaching (GSB) signal is proportional to the number of photocarriers in the excited state.

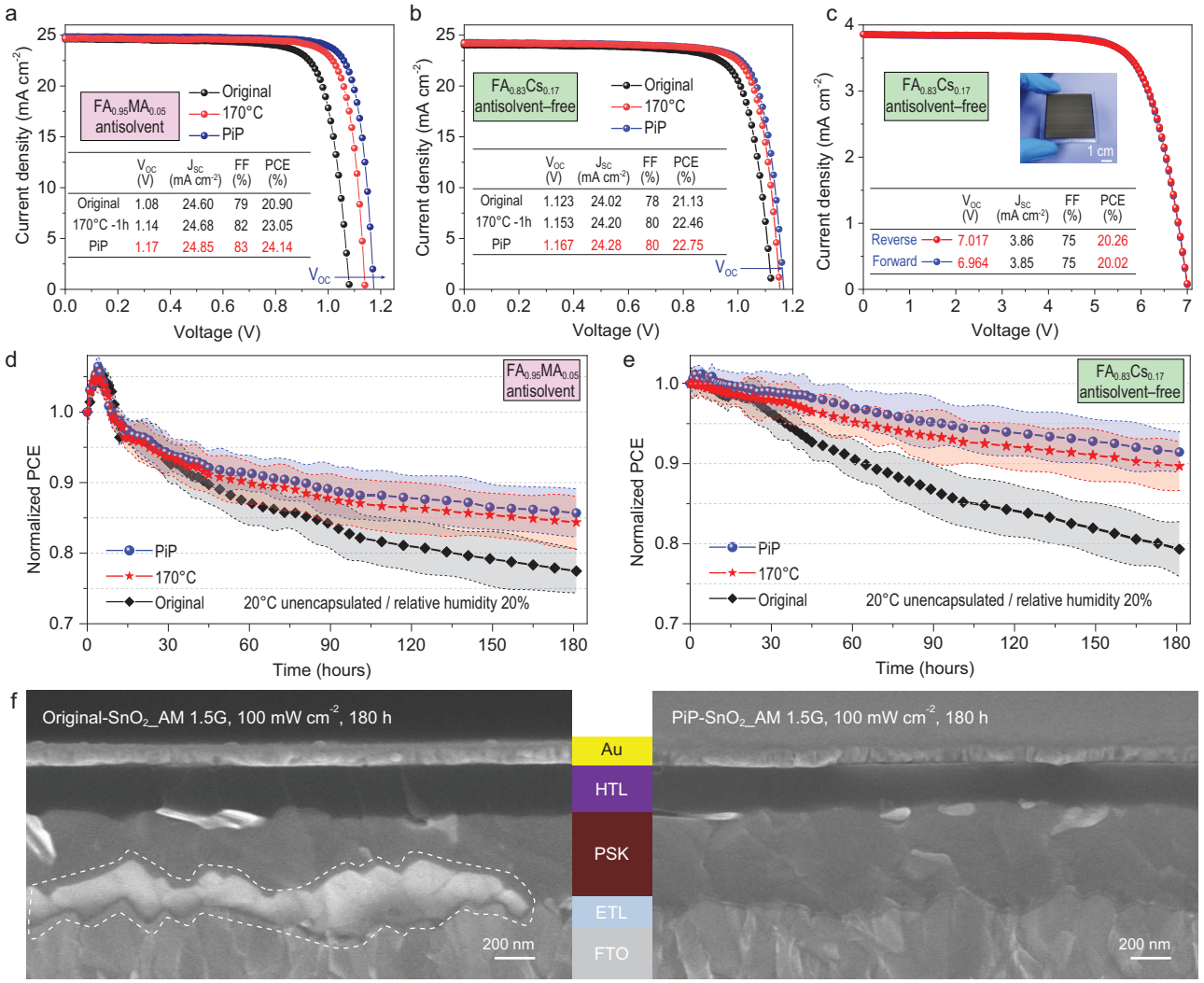

Figure 4. Universality and scalability of PiP for PSCs and performance comparison of PSCs. (a) *J–V* curves and photovoltaic parameters of a representative antisolvent-processed PSC that used original-SnO_2/$FA_{0.95}MA_{0.05}$, 170°C-SnO_2/$FA_{0.95}MA_{0.05}$ and PiP-SnO_2/$FA_{0.95}MA_{0.05}$. (b) *J–V* curves and photovoltaic parameters of a representative antisolvent-free-processed PSC that used original-SnO_2/$FA_{0.83}Cs_{0.17}$, 170°C-SnO_2/$FA_{0.83}Cs_{0.17}$ and PiP-SnO_2/$FA_{0.83}Cs_{0.17}$. (c) *J–V* curves of the PSM recorded in the lab using a mask with an aperture area of 12 cm^2. Average PCE evolution of the unencapsulated (d) $FA_{0.95}MA_{0.05}$ and (e) $FA_{0.83}Cs_{0.17}$ devices measured over a 180-h stability test under light soaking with AM1.5G-simulated illumination (RH $\sim$ 20 $\pm$ 5%). The shaded regions represent the variation range of the PCE obtained from six cells. (f) Cross-sectional SEM images of original-SnO_2/$FA_{0.83}Cs_{0.17}$/i-BABr/spiro/Au and PiP-SnO_2/$FA_{0.83}Cs_{0.17}$/i-BABr/spiro/Au aged under continuous AM1.5G-simulated illumination for 180 hours. The degraded area of the perovskite film at the SnO_2/perovskite interface is marked by the dashed line.

This signal decays when the perovskite undergoes electron-hole recombination or charge transfer to an accepting layer [35]. It can be clearly seen that the GSB signal of the perovskite based on the PiP-SnO_2 decays faster compared with the other two samples in the same timescale, which supports the more rapid charge transfer to the SnO_2 ETL [36]. The decay traces of SnO_2/perovskite have been well fitted with a three-exponential function (Fig. 3e) and the relevant decay time constants are collected in the inserted table. As shown in Fig. 3f, the fastest time constant τ_1 more likely arises from the excitation of electrons [37]. The faster time constant τ_2 is plausibly attributed to the electron transfer from the photoexcited perovskite to the SnO_2 conduction band, while the slowest time constant τ_3 is all within 400–600 ps, which can be ascribed to the charge recombination dynamics of the perovskite as reported previously [38,39]. The τ_2 for the PiP-SnO_2/perovskite film is much shorter, which indicates the significant enhancement of the electron-transfer rate $(1/\tau_2)$. There is a slight increase in τ_3, indicating that the electrons can survive for a longer time in the PiP-SnO_2-based perovskite.

Universality and scalability of PiP for PSCs

To evaluate the effect of the PiP of the SnO_2 thin film on cell performance, we fabricated antisolvent-processed PSCs that have the layered architecture $FTO/SnO_2/(FAPbI_3)_{0.95}(MAPbBr_3)_{0.05}$ $(FA_{0.95}MA_{0.05})$/spiro-OMeTAD/Au, where MA is methylammonium and FA refers to formamidinium. The typical current density–voltage (J–V) curves are shown in Fig. 4a and Supplementary Figs S13 and S14a–c. It is worth noting that the hysteresis is suppressed after the PiP. The PiP-SnO_2-based PSCs achieve a champion PCE of 24.14%, with an open-circuit voltage (V_{OC}) of 1.17 V, a J_{SC} of 24.85 mA cm^{-2} and a fill factor (FF) of 0.83. The corresponding stabilized power output (SPO) is 23.53% for the PiP-SnO_2-based devices (Supplementary Fig. S14d) and the statistical distributions of the photovoltaic parameters are plotted in Supplementary Fig. S15. The external quantum efficiency (EQE) spectra of corresponding perovskite devices well match with the J_{SC} measured by using the J–V curves (Supplementary Fig. S16).

To prove that the PiP of SnO_2 is a universally applicable methodology, we fabricated PSCs with another type of perovskite by using antisolvent-free processing, $FA_{0.83}Cs_{0.17}PbI_{3-x}Cl_x$ $(FA_{0.83}Cs_{0.17})$. The representative J–V curves and corresponding SPOs are compared in Fig. 4b and Supplementary Fig. S17, and the statistical result is shown in Supplementary Fig. S18. The corresponding EQE spectra show an integrated J_{SC} of 23.94 and 23.73 mA cm^{-2} for devices with and without PiP, respectively (Supplementary Fig. 19), which match well with the measured J_{SC}. For the cell using PiP-SnO_2, we achieve a PCE of 22.75% with negligible hysteresis. The FF increases from 78% to 80% and the V_{OC} increases from 1.123 to 1.167 V. To demonstrate the scalability of this approach, we fabricated PSMs consisting of 6-sub cells connected in series and obtained a PCE of 20.26% on an aperture area of 12 cm^2 with a high geometric FF (~97.7%) by precise control of the P1–P2–P3 process (the J–V curves and a photograph of the PSM are shown in Fig. 4c). The details of the PSM architecture and the statistical result of the PCE are shown in Supplementary Fig. S20. An obvious increase in V_{OC} for both $FA_{0.95}MA_{0.05}$, $FA_{0.83}Cs_{0.17}$ and $FA_{0.83}Cs_{0.17}$ PSMs is observed in Supplementary Fig. S21, which can be attributed to the reduction in the charge recombination at the SnO_2/perovskite interface. In addition, PSCs using PiP-SnO_2 also have improved performance compared with PSCs using SnO_2 conventionally annealed at 170°C-SnO_2. Furthermore, as shown in Fig. 4d and e, the long-term stability of the devices with PiP-SnO_2 under light soaking with AM1.5G-simulated illumination at a temperature of 20 ± 5°C is greatly enhanced compared with other annealing conditions when stored under ambient air conditions with 20% ± 5% relative humidity (RH) without encapsulation over 180 hours. Upon introducing the PiP strategy to passivate the SnO_2 layer, the bulk morphology of the SnO_2/perovskite bilayer featuring well-defined interfaces is markedly stabilized under continuous AM1.5G-simulated illumination for 180 hours (Fig. 4f and Supplementary Fig. S22). Taken together, our results suggest that the PiP of SnO_2 is an effective and universal approach to significantly enhance PSC performance and facilitates the scale-up of PSCs.

CONCLUSION

In summary, in this study, we developed a novel non-equilibrium PiP technique for the low-temperature fabrication of PSCs. The ultrafast and efficient electron–electron and electron–phonon scattering ensure room-temperature annealing of SnO_2 nanoparticle-based ETLs prepared by using CBD with an ultrafast heating rate, which efficiently passivates the surface and bulk defects of SnO_2. By rapidly scanning a laser beam, the annealing process at room temperature can be finished in a few minutes, which normally takes hours by continuous thermal annealing at 170°C, reducing the energy cost and fabrication time. Our PiP technique has been demonstrated to be a universal and scalable approach in different types of PSCs and PSMs, and shows significantly enhanced performance in both PCE and stability (Supplementary Table S2). This study establishes a new approach towards the commercialization of efficient low-temperature manufacturing of PSCs.

METHODS

SnO_2 ETL fabrication

The FTO substrate was first etched by using a femtosecond laser scanning system and then cleaned by sonicating in detergent, deionized water and ethyl alcohol for 30 min each. The CBD solution was prepared by dissolving 5 g of urea, 100 μL of mercaptoacetic acid and 5 mL of HCl (37 wt%) into 400 mL of deionized water and then adding 1.096 g of $SnCl_2 \cdot 2H_2O$ to the solution (0.012 M). The cleaned FTO substrate was immersed in the diluted CBD solution (0.002 M) and reacted at 90°C. After 3 hours, the SnO_2 deposited FTO substrate was

washed by sonicating in deionized water for 5 min. The thus prepared SnO_2 thin film was then processed under different annealing conditions.

The home-built PiP set-up

A femtosecond laser source (TANGOR-100 W, Amplitude) with a center wavelength of 1030/515 nm, pulse duration of ∼425 fs and oscillator frequency close to 40 MHz was integrated into a polygon laser scanning system (LSE300 STD, Next scan technology) that was equipped with a high-precision linear stage (PRO165LM, Aerotech). An attenuator (2-EWP-R-0515-M, Altechna) was placed in the optical path to adjust the laser pulse energy fluence. The polygon laser scanning speed could be up to 100 m s^{-1}. To measure the exact pulse energy, a photodiode power meter was used (S120VC, Thorlabs). The in-scan resolution and the cross-scan resolution were set to 0.9 and 20 μm, respectively, so that the laser spot (45 μm) could fully cover the sample. The laser scanning speed was 36 m s^{-1} and the stage moving speed was 1.66 mm s^{-1}.

PSM laser etching

P1, P2 and P3 were all scribed by using a femtosecond laser machine (Pharos-10 W, light conversion). The FTO glass was first etched to form the module substrate with six strips (P1) with a laser power of 0.15 W, pulse duration of 10 ps, repetition rate of 10 KHz and laser scanning speed of 250 mm s^{-1}. After the deposition of the spiro-OMeTAD film, the sample was re-etched to form P2 lines with a laser power of 0.3 W, pulse duration of 2 ps, repetition rate of 200 KHz and laser scanning speed of 500 mm s^{-1}. Finally, an effective series of connected modules was formed by etching the Au to form P3 lines with a laser power of 5 mW, pulse duration of 260 fs, repetition rate of 1 KHz and laser scanning speed of 20 mm s^{-1}. With precise control of the P1–P2–P3 process, we achieved a high geometric FF (∼97.7%).

SUPPLEMENTARY DATA

Supplementary data are available at *NSR* online.

ACKNOWLEDGEMENTS

This S/TEM work was performed at the Nanostructure Research Center, which is supported by the State Key Laboratory of Advanced Technology for Materials Synthesis and Processing, and the State Key Laboratory of Silicate Materials for Architectures (all of the laboratories are at Wuhan University of Technology).

FUNDING

This work was supported by the National Key Research and Development Program of China (2020YFA0715000), the Foshan Xianhu Laboratory of the Advanced Energy Science and Technology Guangdong Laboratory (XHT2020-005) and the Guangdong Basic and Applied Basic Research Foundation (2020A1515110250 and 2021B1515120041).

AUTHOR CONTRIBUTIONS

X.W. conceived the idea. N.C. and X.C. designed, realized and tested the measurement unit. Z.Z. contributed to the ultrafast pump-probe transient absorption measurements. R.Y, Y.Y. and B.M. contributed to TEM, SEM and XRD measurement. J.W., L.M. and Y.C. support the data analysis. N.C., X.C. and X.W. wrote and revised the manuscript.

Conflict of interest statement. None declared.

REFERENCES

1. Chen H, Wang Y and Fan Y *et al.* Decoupling engineering of formamidinium–cesium perovskites for efficient photovoltaics. *J Phys Chem Lett* 2022; **9**: 5962–9.
2. Chen C, Chen J and Han H *et al.* Perovskite solar cells based on screen-printed thin films. *Nature* 2022; **612**: 266–71.
3. You S, Zeng H and Liu Y *et al.* Radical polymeric p-doping and grain modulation for stable, efficient perovskite solar modules. *Science* 2023; **379**: 288–94.
4. Yang T, Ma C and Cai W *et al.* Amidino-based Dion-Jacobson 2D perovskite for efficient and stable 2D/3D heterostructure perovskite solar cells. *Joule* 2023; **7**: 574–86.
5. Li D, Shi J and Xu Y *et al.* Inorganic-organic halide perovskites for new photovoltaic technology. *Natl Sci Rev* 2018; **5**: 559–76.
6. Luo L, Zeng H and Wang Z *et al.* Stabilization of 3D/2D perovskite heterostructures via inhibition of ion diffusion by cross-linked polymers for solar cells with improved performance. *Nat Energy* 2023; **8**: 294–303.
7. Yoo JJ, Seo G and Chua MR *et al.* Efficient perovskite solar cells via improved carrier management. *Nature* 2021; **590**: 587–93.
8. Yu Z, Yang Z and Ni Z *et al.* Simplified interconnection structure based on C_{60}/SnO_{2-x} for all-perovskite tandem solar cells. *Nat Energy* 2020; **5**: 657–65.
9. Kim M, Jeong J and Lu H *et al.* Conformal quantum dot-SnO_2 layers as electron transporters for efficient perovskite solar cells. *Science* 2022; **375**: 302–6.
10. Bu T, Ono LK and Li J *et al.* Modulating crystal growth of formamidinium-caesium perovskites for over 200 cm^2 photovoltaic sub-modules. *Nat Energy* 2022; **7**: 528–36.
11. Bu T, Li J and Li H *et al.* Lead halide-templated crystallization of methylamine-free perovskite for efficient photovoltaic modules. *Science* 2021; **372**: 1327–32.
12. Min H, Lee DY and Kim J *et al.* Perovskite solar cells with atomically coherent interlayers on SnO_2 electrodes. *Nature* 2021; **598**: 444–50.
13. Park J, Kim J and Yun H-S *et al.* Controlled growth of perovskite layers with volatile alkylammonium chlorides. *Nature* 2023; **616**: 724–30.

14. Lee JH, Lee S and Kim T *et al.* Interfacial α-$FAPbI_3$ phase stabilization by reducing oxygen vacancies in SnO_{2-x}. *Joule* 2023; **7**: 380–97.
15. Park SY and Zhu K. Advances in SnO_2 for efficient and stable n-i-p perovskite solar cells. *Adv Mater* 2022; **34**: 2110438.
16. Jeong MJ, Moon CS and Lee S *et al.* Boosting radiation of stacked halide layer for perovskite solar cells with efficiency over 25%. *Joule* 2023; **7**: 112–27.
17. Haghighi M, Ghazyani N and Mahmoodpour S *et al.* Low-temperature processing methods for tin oxide as electron transporting layer in scalable perovskite solar cells. *Sol RRL* 2023; **7**: 2201080.
18. Reddy SH, Di Giacomo F and Di Carlo A. Low-temperature-processed stable perovskite solar cells and modules: a comprehensive review. *Adv Energy Mater* 2022; **12**: 2103534.
19. Huang L, Lou Y-H and Wang Z-K. Buried interface passivation: a key strategy to breakthrough the efficiency of perovskite photovoltaics. *Small* 2023; **19**: 2302585.
20. Han T-H, Tan S and Xue J *et al.* Interface and defect engineering for metal halide perovskite optoelectronic devices. *Adv Mater* 2019; **31**: 1803515.
21. Sundaram SK and Mazur E. Inducing and probing non-thermal transitions in semiconductors using femtosecond laser pulses. *Nat Mater* 2002; **1**: 217–24.
22. Kwon H, Baik S and Jang JE *et al.* Ultra-short pulsed laser annealing effects on MoS_2 transistors with asymmetric and symmetric contacts. *Electron* 2019; **8**: 222.
23. Liu W, Luo J and Li S *et al.* The seeds and homogeneous nucleation of photoinduced nonthermal melting in semiconductors due to self-amplified local dynamic instability. *Sci Adv* 2022; **8**: eabn4430.
24. Tang E, Lin X and Gao G *et al.* Experimental research on temperature field distributions for optical lenses irradiated by femtosecond laser. *Opt Laser Technol* 2018; **106**: 251–8.
25. Song C, Yang H and Liu F *et al.* Ultrafast femtosecond pressure modulation of structure and exciton kinetics in 2D halide perovskites for enhanced light response and stability. *Nat Commun* 2021; **12**: 4879.
26. Chen Y, Zuo X and He Y *et al.* Dual passivation of perovskite and SnO_2 for high-efficiency $MAPbI_3$ perovskite solar cells. *Adv Sci* 2021; **8**: 2001466.
27. Jung EH, Chen B and Bertens K *et al.* Bifunctional surface engineering on SnO_2 reduces energy loss in perovskite solar cells. *ACS Energy Lett* 2020; **5**: 2796–801.
28. Huster N, Zanders D and Karle S *et al.* Additive-free spin coating of tin oxide thin films: synthesis, characterization and evaluation of tin β-ketoiminates as a new precursor class for solution deposition processes. *Dalton Trans* 2020; **49**: 10755–64.
29. Jiang E, Ai Y and Yan J *et al.* Phosphate-passivated SnO_2 electron transport layer for high-performance perovskite solar cells. *ACS Appl Mater Interfaces* 2019; **11**: 36727–34.
30. Costa IM, Colmenares YN and Pizani PS *et al.* Sb doping of VLS synthesized SnO_2 nanowires probed by Raman and XPS spectroscopy. *Chem Phys Lett* 2018; **695**: 125–30.
31. Drabeski RG, Gunha JV and Novatski A *et al.* Raman and photoacoustic spectroscopies of SnO_2 thin films deposited by spin coating technique. *Vib Spectrosc* 2020; **109**: 103094.
32. Qian Z, Chen L and Wang J *et al.* Manipulating SnO_2 growth for efficient electron transport in perovskite solar cells. *Adv Mater Interfaces* 2021; **8**: 2100128.
33. Zhuang J, Mao P and Luan Y *et al.* Rubidium fluoride modified SnO_2 for planar n-i-p perovskite solar cells. *Adv Funct Mater* 2021; **31**: 2010385.
34. Tu B, Shao Y and Chen W *et al.* Novel molecular doping mechanism for n-doping of SnO_2 via triphenylphosphine oxide and its effect on perovskite solar cells. *Adv Mater* 2019; **31**: 1805944.
35. Tvrdy K, Frantsuzov PA and Kamat PV. Photoinduced electron transfer from semiconductor quantum dots to metal oxide nanoparticles. *Proc Natl Acad Sci USA* 2011; **108**: 29–34.
36. Zhong J, Wu W and Zhou Y *et al.* Room temperature fabrication of SnO_2 electrodes enabling barrier-free electron extraction for efficient flexible perovskite photovoltaics. *Adv Funct Mater* 2022; **32**: 2200817.
37. Zhang P, Zhu G and Shi Y *et al.* Ultrafast interfacial charge transfer of cesium lead halide perovskite films $CsPbX_3$ (X = Cl, Br, I) with different halogen mixing. *J Phys Chem C* 2018; **122**: 27148–55.
38. Huang S-K, Wang Y-C and Ke W-C *et al.* Unravelling the origin of the photocarrier dynamics of fullerene-derivative passivation of SnO_2 electron transporters in perovskite solar cells. *J Mater Chem A* 2020; **8**: 23607–16.
39. Scheidt RA, Kerns E and Kamat PV. Interfacial charge transfer between excited $CsPbBr_3$ nanocrystals and TiO_2: charge injection versus photodegradation. *J Phys Chem Lett* 2018; **9**: 5962–9.